

# Sparse Bayesian mass-mapping with uncertainties: hypothesis testing of structure

M. A. Price<sup>1</sup>\*, J. D. McEwen<sup>1</sup>, X. Cai<sup>1</sup>, T. D. Kitching<sup>1</sup>, C. G. R. Wallis<sup>1</sup>

(for the LSST Dark Energy Science Collaboration)

<sup>1</sup>*Mullard Space Science Laboratory, University College London, RH5 6NT, UK.*

Accepted XXX. Received YYY; in original form ZZZ

## ABSTRACT

A crucial aspect of mass-mapping, via weak lensing, is quantification of the uncertainty introduced during the reconstruction process. Properly accounting for these errors has been largely ignored to date. We present a new method to reconstruct *maximum a posteriori* (MAP) convergence maps by formulating an unconstrained Bayesian inference problem with Laplace-type  $l_1$ -norm sparsity-promoting priors, which we solve via convex optimization. Approaching mass-mapping in this manner allows us to exploit recent developments in probability concentration theory to infer theoretically conservative uncertainties for our MAP reconstructions, without relying on assumptions of Gaussianity. For the first time these methods allow us to perform hypothesis testing of structure, from which it is possible to distinguish between physical objects and artifacts of the reconstruction. Here we present this new formalism, demonstrate the method on simulations, before applying the developed formalism to two observational datasets of the Abel-520 cluster. Initial reconstructions of the Abel-520 catalogs reported the detection of an anomalous ‘dark core’ – an over dense region with no optical counterpart – which was taken to be evidence for self-interacting dark-matter. In our Bayesian framework it is found that neither Abel-520 dataset can conclusively determine the physicality of such dark cores at 99% confidence. However, in both cases the recovered MAP estimators are consistent with both sets of data.

**Key words:** gravitational lensing: weak – (*Cosmology:*) dark matter – methods: statistical – methods: data analysis – techniques: image processing

## 1 INTRODUCTION

Gravitational lensing is an astrophysical phenomenon, that can be observed on galactic to cosmic spatial scales, through which distant images are distorted by the intervening mass density field. Due to its nature, lensing is sensitive to the total mass distribution (both visible and invisible) along a line of sight (Bartelmann & Schneider 2001; Schneider 2005; Munshi et al. 2008; Heavens 2009). Therefore, as the majority of massive structures in the universe are predominantly dark matter, lensing provides a novel way to probe the nature of dark matter itself. Weak gravitational lensing (WL) is a regime in which one makes the approximation that lensed sources have (at no time) come radially closer than an Einstein radius to the intervening mass concentrations – which ensures that sources are not multiply imaged. The effect of weak lensing on distant source galaxies is two-fold: the galaxy size is magnified by a convergence field  $\kappa$ ; and the galaxy ellipticity (third-flattening) is perturbed from an underlying intrinsic value by a shearing field  $\gamma$ .

Due to the mass-sheet degeneracy the weak lensing convergence field is not directly observable. In the weak lensing regime, the shearing field does not suffer such degeneracies and can accurately be modelled from observed ellipticities. Therefore, observations of  $\gamma$  are typically inverted to recover estimators of  $\kappa$ . Such estimators are colloquially named *dark matter mass-maps*, and constitute one of the principle observables for cosmology (Clowe et al. 2006). Standard cosmological protocol is to extract weak lensing information in the form of second order statistics (Alsing et al. 2016; Taylor et al. 2018; Kilbinger 2015) which are then compared to theory. In this approach mass-maps are not required. However, as two-point global statistics are by definition sensitive only to Gaussian contributions, and weak lensing is inherently non-Gaussian, it is informative to consider higher-order statistics (Munshi & Coles 2017; Coles & Chiang 2000). Many higher-order statistical techniques can be performed directly on mass-maps ( $\kappa$ -fields), which motivates investigation into alternate mass-map reconstruction methodologies.

Reconstructing mass-maps from shear observations requires solving an ill-posed (often seriously) inverse problem. Many approaches to solving this lensing inverse problem have been developed (*e.g.* VanderPlas et al. 2011; Kaiser & Squires 1993; Lanusse

\* E-mail: m.price.17@ucl.ac.uk

## 2 Price et al.

et al. 2016; Wallis et al. 2017; Jeffrey et al. 2018; Chang et al. 2018), with the industry standard being Kaiser-Squires (KS, Kaiser & Squires 1993). Although these approaches often produce reliable convergence estimators, they lack principled statistical approaches to uncertainty quantification and often assume Gaussianity during the reconstruction process, or post-process by Gaussian smoothing, which is sub-optimal when one wishes to analyze small-scale non-Gaussian structure.

Most methods refrain from quantifying uncertainties in reconstructions, but those that do often do so by assuming Gaussian priors and adopting Markov-chain Monte-Carlo (MCMC) techniques (Corless et al. 2009; Alsing et al. 2016; Schneider et al. 2015). The computational cost of MCMC approaches is large. Recent developments in probability concentration theory have led to advancements in fast approximate uncertainty quantification techniques (Pereyra 2017; Cai et al. 2017a,b).

In this article we present a new mass-mapping formalism. We formulate the lensing inverse problem as a sparse hierarchical Bayesian inference problem from which we derive an unconstrained convex optimization problem. We solve this optimization problem in the analysis setting, with a wavelet-based, sparsity-promoting,  $l_1$ -norm prior – similar priors have been shown to be effective in the weak lensing setting (Jeffrey et al. 2018; Lanusse et al. 2016; Peel et al. 2017; Leonard et al. 2014). Formulating the problem in this way allows us, for the first time, to recover *maximum a posteriori* (MAP) estimators, from which we can exploit analytic methods (Pereyra 2017; Cai et al. 2017b) to recover approximate highest posterior density (HPD) credible regions, and perform hypothesis testing of structure in a variety of ways. We apply our algorithm to a range of catalogs drawn from N-body simulations – Bolshoi cluster catalogues (Klypin et al. 2011) – and the debated A520 cluster catalogs (Clowe et al. 2012; Jee et al. 2014). We then demonstrate the aforementioned uncertainty quantification techniques on our MAP reconstructions from these catalogs.

The structure of this article is as follows. In section 2 we provide a brief overview of the weak lensing paradigm and motivate a sparsity-based approach. In section 3 we provide the details of our algorithm, as well as some updates to super-resolution image recovery. In section 4 we present the uncertainty quantification techniques, both mathematically and mechanistically. In sections 5 and 6 we apply both our reconstruction algorithm and the uncertainty quantification techniques to the aforementioned datasets and analyze the results. Finally, in section 7 we draw conclusions from this work and propose future avenues of research.

Section 3 relies on a moderate level of understanding in the fields of proximal calculus and compressed sensing, and section 4 relies on a general understanding of Bayesian inference. As such, for the reader solely interested in practical application of these techniques we recommend sections 5 onwards.

## 2 WEAK GRAVITATIONAL LENSING

The following section presents a brief review of the mathematical background relevant to the weak lensing formalism, though a deeper description can be found in popular review articles (Bartelmann & Schneider 2001; Schneider 2005).

### 2.1 Weak lensing regime

Gravitational lensing refers to the deflection of distant photons as they propagate from their origin to us, the observer. This deflection is

caused by local Newtonian potentials which are, in turn, sourced by the total local matter over or under density. As such, weak lensing is sensitive to both the visible and invisible matter distribution – making it an ideal probe of dark matter in the Universe.

The weak gravitational lensing regime is satisfied when propagating photons (from a distant source) have an angular position on the source plane  $\beta$  (relative to the line-of-sight from observer through the lensing mass) greater than the Einstein radius  $\theta_E$  of the intervening mass. This assertion ensures that the solution of the first order lens equation is singular:

$$\beta = \theta - \theta_E^2 \frac{\theta}{|\theta|^2}. \quad (1)$$

Where the Einstein radius is defined to be:

$$\theta_E = \sqrt{\frac{4GM}{c^2} \frac{f_K(r-r')}{f_K(r)f_K(r')}}, \quad (2)$$

where  $f_K$  is the angular diameter distance in a cosmology with curvature  $K$ ,  $c$  is the speed of light in a vacuum,  $G$  is the gravitational constant and  $M$  is the lensing mass. Perhaps more generally the weak lensing regime can be defined as convergence fields for which  $\kappa \ll 1$  – ensuring that the shear signal remains linear.

Due to the sparse nature of the distribution of galaxies across the sky, most sources are (to a good approximation) within the weak gravitational lensing regime. The weak gravitational lensing effect is best expressed in terms of a lensing potential  $\phi$ , defined to be the integral of the Newtonian potential  $\Phi$  along a given line of sight:

$$\phi(r, \omega) = \frac{2}{c^2} \int_0^r dr' \frac{f_K(r-r')}{f_K(r)f_K(r')} \Phi(r', \omega), \quad (3)$$

where  $r$  and  $r'$  are co-moving distances, and  $\omega = (\theta, \psi)$  are angular spherical co-ordinates. The local Newtonian potential must satisfy the Poisson equation and as such is related to the matter over-density field:

$$\nabla^2 \Phi(r, \omega) = \frac{3\Omega_M H_0^2}{2a(r)} \delta(r, \omega), \quad (4)$$

where  $\Omega_M$  is the matter density parameter,  $H_0$  is the current Hubble constant,  $a(r)$  is the scale factor, and  $\delta$  is the fractional over-density.

To first order, there are two primary ways in which light from distant sources is distorted by this lensing potential. Images are magnified by a spin-0 convergence field  $\kappa$  and sheared by a spin-2 shear field  $\gamma$ . These quantities can be shown (Bartelmann & Schneider 2001) to be related to the lensing potential by:

$$\kappa(r, \omega) = \frac{1}{4} (\delta \bar{\delta} + \bar{\delta} \delta) \phi(r, \omega), \quad (5)$$

$$\gamma(r, \omega) = \frac{1}{2} \delta \bar{\delta} \phi(r, \omega), \quad (6)$$

where  $\delta$  and  $\bar{\delta}$  are the spin  $s$  raising and lowering operators respectively and are in general defined to be,

$$\delta \equiv -\sin^s \theta \left( \frac{\partial}{\partial \theta} + \frac{i\partial}{\sin \theta \partial \psi} \right) \sin^{-s} \theta, \quad (7)$$

$$\bar{\delta} \equiv -\sin^{-s} \theta \left( \frac{\partial}{\partial \theta} - \frac{i\partial}{\sin \theta \partial \psi} \right) \sin^s \theta. \quad (8)$$

Where we have omitted spin subscripts for clarity.

## 2.2 Standard mass-mapping techniques

Typically we wish to make inferences about the projected matter over-density  $\delta(r, \omega)$  which is most directly accessible by inverting the integral equation (Schneider 2005)

$$\kappa(r, \omega) = \frac{3\Omega_M H_0^2}{2c^2} \int_0^r dr' \frac{f_K(r') f_K(r - r')}{f_K(r)} \frac{\delta(f_K(r') r', r')}{a(r)}. \quad (9)$$

This poses a difficulty as the convergence  $\kappa$  is only determined to the degeneracy  $\kappa \rightarrow \kappa' = \eta\kappa + (1 - \eta)$  and is therefore not directly observable — this degeneracy is often referred to as the *mass-sheet degeneracy*. However, as the intrinsic ellipticity distribution of galaxies has zero mean, if one averages many galaxy ellipticities within a given pixel the true shear  $\gamma$  can be recovered — which makes  $\gamma$  an observable field. As such one typically collects observations of  $\gamma$  which are and subsequently used to construct estimators of  $\kappa$ .

For small sky fractions we can approximate the field of view as a plane (though this approximation degrades quickly with sky fraction; Wallis et al. 2017). In this planar approximation  $\delta$  and  $\bar{\delta}$  reduce to (Bunn et al. 2003a):

$$\delta \approx -(\partial_x + i\partial_y) \quad \text{and} \quad \bar{\delta} \approx -(\partial_x - i\partial_y). \quad (10)$$

Combining equations (5) and (6) we find the planar forward model in Fourier space:

$$\hat{\gamma}(k_x, k_y) = \mathbf{D}_{k_x, k_y} \hat{\kappa}(k_x, k_y), \quad (11)$$

with the mapping operator being,

$$\mathbf{D}_{k_x, k_y} = \frac{k_x^2 - k_y^2 + 2ik_x k_y}{k_x^2 + k_y^2}. \quad (12)$$

Hereafter we drop the  $k_x, k_y$  subscripts for clarity. It is informative to note that this forward model is undefined at the origin ( $k = \sqrt{k_x^2 + k_y^2} = 0$ ) — which corresponds to the mass-sheet degeneracy (Bartelmann & Schneider 2001).

The most naive inversion of this forward model is Kaiser-Squires (KS) inversion,

$$\hat{\kappa}^{\text{KS}} = \mathbf{D}^{-1} \hat{\gamma}, \quad (13)$$

which is direct inversion in Fourier space (Kaiser & Squires 1993). KS inversion of the forward model, given by equation (11), performs adequately, provided the space over which it is defined is complete, and the sky fraction is small. However, masking and survey boundaries are inherent in typical weak gravitational lensing surveys, leading to significant contamination of the KS estimator. Often maps recovered with the KS estimator are convolved with a Gaussian kernel to reduce the impact of these contaminations but this is sub-optimal. This smooths away a large fraction of the small-scale non-Gaussian information, which cosmologists are increasingly interested in extracting from weak gravitational lensing surveys.

## 3 SPARSE MAP ESTIMATORS

Several alternate approaches for solving the inverse problem between convergence  $\kappa$  and shear  $\gamma$  which do not assume or impose Gaussianity have been proposed, some of which are based on the concept of wavelets and sparsity (Lanusse et al. 2016; Pires et al. 2009; Jullo et al. 2014; Peel et al. 2017).

We propose a mass-mapping algorithm that relies on sparsity

in a given wavelet dictionary. Moreover, we formulate the problem such that we can exploit recent developments in the theory of probability concentration, which have been developed further to produce novel uncertainty quantification techniques (Pereyra 2017). Crucially, this allows us to recover principled statistical uncertainties on our MAP reconstructions (as in Cai et al. 2017a,b) as will be discussed in detail in the following section.

As mentioned previously, galaxies have an intrinsic ellipticity. To mitigate the effect of intrinsic ellipticity we choose to project the ellipticity measurements onto a grid and average. If we assume that galaxies have no preferential orientation in the absence of lensing effects, then the average intrinsic ellipticity tends to zero. This is a good approximation for the purposes of this paper, but weak correlation between the intrinsic alignments of galaxies has been observed (Troxel & Ishak 2015; Piras et al. 2018).

## 3.1 Hierarchical Bayesian Framework

Hierarchical Bayesian inference provides a rigorous mathematical framework through which theoretically optimal solutions can be recovered. Moreover it allows one to construct measures of the uncertainty on recovered point estimates.

As is common for hierarchical Bayesian models, we begin from Bayes’ theorem for the posterior distribution,

$$p(\kappa|\gamma) = \frac{p(\gamma|\kappa)p(\kappa)}{\int_{\mathbb{C}^N} p(\gamma|\kappa)p(\kappa)d\kappa}, \quad (14)$$

where  $p(\gamma|\kappa)$  is the likelihood function representing data fidelity,  $N$  is the dimensionality of  $\kappa$  and  $p(\kappa)$  is a prior on the statistical nature of  $\kappa$ . The denominator is called the *Bayesian evidence* which is constant and so can be dropped for our purposes. Typically the Bayesian evidence is used for model comparison, which we will not be considering within the context of this paper. Given Bayes’ theorem, and the monotonicity of the logarithm function, we can easily show that the maximum posterior solution is defined by,

$$\underset{\kappa}{\operatorname{argmax}}\{p(\kappa|\gamma)\} = \underset{\kappa}{\operatorname{argmin}}\{-\log(p(\kappa|\gamma))\}. \quad (15)$$

This step is crucial, as it allows us to solve the more straightforward problem of minimizing the log-posterior rather than maximizing the full posterior. Conveniently, in most physical situations the operators associated with the log-posterior are convex. Drawing from the field of convex optimization, the optimal solution for the posterior can be recovered extremely quickly — even in high dimensional settings.

## 3.2 Sparsity and Inverse problems

Let  $\gamma \in \mathbb{C}^M$  be the discretized complex shear field extracted from an underlying discretized convergence field  $\kappa \in \mathbb{C}^N$  by a measurement operator  $\Phi \in \mathbb{C}^{M \times N} : \kappa \mapsto \gamma$ . In the planar setting  $\Phi$  can be modeled by,

$$\Phi = \mathbf{M}\mathbf{F}^{-1}\mathbf{D}\mathbf{F}. \quad (16)$$

Here  $\mathbf{F}$  is the discrete fast Fourier transform (FFT),  $\mathbf{F}^{-1}$  is the inverse discrete fast Fourier transform (IFFT),  $\mathbf{M}$  is a standard masking operator, and  $\mathbf{D}$  is a diagonal matrix applying the scaling of the forward model in Fourier space as defined in equation (12). In the case of independent and identically distributed *i.i.d.* Gaussian noise, measurement of  $\gamma$  will be contaminated such that:

$$\gamma = \Phi\kappa + \mathcal{N}(0, \sigma_i^2), \quad (17)$$

where  $\mathcal{N}(0, \sigma_i^2) \in \mathbb{C}^M$  is additive i.i.d. Gaussian noise of variance  $\sigma_i^2$  for pixel  $i$ . Often in weak gravitational lensing experiments the total number of binned measurements is less than the number of pixels to be recovered,  $M < N$ , and the inverse problem becomes ill-posed.

In such a setting the Bayesian likelihood function (data fidelity term) is given by the product of Gaussian likelihoods defined on each pixel with pixel noise variance  $\sigma_i^2$ , which is to say an overall multivariate Gaussian likelihood of known covariance  $\Sigma = \text{diag}(\sigma_1, \sigma_2, \dots, \sigma_M) \in \mathbb{R}^{M \times M}$ . Let  $\Phi_i \kappa$  be the value of  $\Phi \kappa$  at pixel  $i$ , then the overall likelihood is then defined as,

$$\begin{aligned} p(\gamma|\kappa) &\propto \prod_{i=0}^M \exp\left(\frac{-(\Phi_i \kappa - \gamma_i)^2}{2\sigma_i^2}\right) = \prod_{i=0}^M \exp\left(\frac{-1}{2} (\bar{\Phi}_i \kappa - \bar{\gamma}_i)^2\right), \\ &= p(\gamma|\kappa) \propto \exp\left(\frac{-\|\bar{\Phi} \kappa - \bar{\gamma}\|_2^2}{2}\right), \end{aligned} \quad (18)$$

where  $\|\cdot\|_2$  is the  $\ell_2$ -norm and  $\bar{\Phi} = \Sigma^{-\frac{1}{2}} \Phi$  is a composition of the measurement operator and an inverse covariance weighting. Effectively this covariance weighting leads to measurements  $\bar{\gamma} = \Sigma^{-\frac{1}{2}} \gamma$  which whiten the typically non-uniform noise variance in the observational data  $\gamma$ .

This likelihood function allows one to map from the number count of observations per pixel to a corresponding noise variance (assuming an intrinsic ellipticity dispersion of  $\sim 0.37$ ), from which the noise (under and central limit theory argument of Gaussianity) may be correctly incorporated into the reconstruction. In practice this requires only the number density of observations per pixel, which is trivially inferred from raw observational data catalogues.

To regularize this inverse problem, we then define a sparsity promoting Laplace-type prior:

$$p(\kappa) \propto \exp\left(-\mu \|\Psi^\dagger \kappa\|_1\right), \quad (19)$$

where  $\Psi$  is an appropriately selected wavelet dictionary, and  $\mu \in \mathbb{R}_+$  is a regularization parameter – effectively a weighting between likelihood and prior. Note that one may choose any convex log-prior within this formalism *e.g.* an  $\ell_2$ -norm prior from which one essentially recovers Weiner filtering (see Padmanabhan et al. 2003; Horowitz et al. 2018, for alternate iterative Weiner filtering approaches). From equations (14) and (15) the unconstrained optimization problem which minimizes the log-posterior is,

$$\kappa^{\text{map}} = \underset{\kappa}{\text{argmin}} \left\{ \mu \|\Psi^\dagger \kappa\|_1 + \frac{\|\bar{\Phi} \kappa - \bar{\gamma}\|_2^2}{2} \right\}, \quad (20)$$

where the bracketed term is called the *objective function*. To solve this convex optimization problem we adopt a forward-backward splitting algorithm (*e.g.* Combettes & Pesquet 2009). A full description of this algorithm applied in the current context is outlined in Cai et al. (2017b).

Let  $f(\kappa) = \mu \|\Psi^\dagger \kappa\|_1$  denote our prior term, and  $g(\kappa) = \|\bar{\Phi} \kappa - \bar{\gamma}\|_2^2/2$  denote our data fidelity term. Then our optimization problem can be re-written compactly as,

$$\underset{\kappa}{\text{argmin}} \{f(\kappa) + g(\kappa)\}. \quad (21)$$

The forward-backward iteration step is then defined to be,

$$\kappa^{(i+1)} = \text{prox}_{\lambda^{(i)} f} \left( \kappa^{(i)} - \lambda^{(i)} \nabla g(\kappa^{(i)}) \right), \quad (22)$$

for iteration  $i$ , with gradient,

$$\nabla g(\kappa) = \bar{\Phi}^\dagger (\bar{\Phi} \kappa - \bar{\gamma}). \quad (23)$$

If the wavelet dictionary  $\Psi$  is a tight frame (*i.e.*  $\Psi^\dagger \Psi = \mathbb{I}$ ) the proximity operator is given by,

$$\text{prox}_{\lambda f} (z) = z + \Psi \left( \text{soft}_{\lambda \mu} (\Psi^\dagger z) - \Psi^\dagger z \right), \quad (24)$$

where  $\text{soft}_\lambda(z)$  is the point-wise soft-thresholding operator (Combettes & Pesquet 2009) and  $\lambda$  is a parameter related to the step-size (which is in turn related to the Lipschitz differentiability of the log-prior) which should be set according to Cai et al. (2017b). The iterative algorithm is given explicitly in the primary iterations of algorithm 1. Adaptations for frames which are not tight can be found in Cai et al. (2017b) and are readily available within our framework.

Our algorithm has distinct similarities to the GLIMPSE algorithm presented by Lanusse et al. (2016), but crucially differs in several aspects. Most importantly we formulate the problem in a hierarchical Bayesian framework which allows us to recover principled statistical uncertainties. In addition to this we include Bayesian inference of the regularization parameter, a robust estimate of the noise-level (which can be folded into the hierarchical model), and we use super-resolution operators instead of non-discrete fast Fourier transforms.

---

**Algorithm 1** Forward-backward analysis algorithm

---

**Input:**  $\gamma \in \mathbb{C}^M$ ,  $\kappa^{(0)} \in \mathbb{C}^N$ ,  $\lambda, \mu^{(0)} = i = t = 0, T_1, T_2 \in \mathbb{R}_+$

**Output:**  $\kappa^{\text{map}} \in \mathbb{C}^N, \mu \in \mathbb{R}_+$

**Precomputation:**

**Do:**

- 1: Calculate  $\kappa^{(t)} = \underset{\kappa}{\text{argmin}} \{f(\kappa) + g(\kappa)\}$ ,
- 2: Update  $\mu^{(t+1)} = \frac{(N/k)+\alpha-1}{f(\kappa^{(t)})+\beta}$ ,
- 3:  $t = t + 1$ ,
- 4: On convergence,  $\mu$  becomes fixed.

**Until:** Iteration limit reached.

**Primary Iterations:**

**Do:**

- 1: update  $\nu^{(i+1)} = \kappa^{(i)} - \lambda \bar{\Phi}^\dagger (\bar{\Phi} \kappa^{(i)} - \bar{\gamma})$ ,
- 2: compute  $\eta = \Psi^\dagger \nu^{(i+1)}$ ,
- 3: update  $\kappa^{(i+1)} = \nu^{(i+1)} + \Psi(\text{soft}_{\lambda \mu}(\eta) - \eta)$ ,
- 4:  $i = i + 1$ .

**Until:** Stopping criterion satisfied.

*i.e.*  $\frac{\|\kappa^{(i)} - \kappa^{(i+1)}\|_2}{\|\kappa^{(i)}\|_2} < T_1$  and  $\frac{\text{obj}(\kappa^{(i)}) - \text{obj}(\kappa^{(i+1)})}{\text{obj}(\kappa^{(i)})} < T_2$ .

---

### 3.3 Reduced Shear

Due to a degeneracy between  $\gamma$  and  $\kappa$  the true observable quantity is in fact the *reduced shear*  $g$  (Bartelmann & Schneider 2001),

$$g = \frac{\gamma}{1 - \kappa}. \quad (25)$$

Deep in the weak lensing regime one can safely approximate  $\gamma \approx g \ll 1$  which ensures that the optimization problem remains linear. However, when reconstructing regions close to massive structures (galaxy clusters) this approximation is no longer strictly valid and we must unravel this additional factor. We adopt the procedure

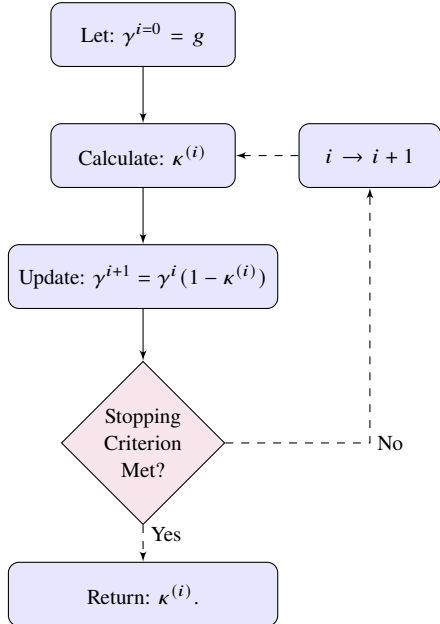


**Figure 1.** Schematic of reduced shear iterations. An initial guess of the MAP solution  $\kappa_i^{\text{map}}$  is constructed, the current best shear estimates  $\gamma_i$  are then used in tandem to construct a new estimate of the true shear field  $\gamma_{i+1}$ .

outlined in Wallis et al. (2017), which we also outline schematically in Figure 1 – this method can be found in detail in Mediavilla et al., pg 153. We find that these corrections typically converge after  $\sim 5\text{-}10$  iterations.

### 3.4 Regularization Parameter Selection

One key issue of sparsity-based reconstruction methods is the selection of the regularization parameter  $\mu$ . Several methodologies have arisen (Lanusse et al. 2016; Peel et al. 2017; Paykari et al. 2014; Jeffrey et al. 2018) for selecting  $\mu$ , though often the regularization parameter is chosen somewhat arbitrarily – as the integrity of the MAP solution is assumed to be weakly dependent on the choice of  $\mu$ . However, to extract principled statistical uncertainties on the recovered images, one must select this parameter in a principled statistical manner.

We apply the hierarchical Bayesian formalism developed by Pereyra et al. (2015) – the details of which are elegantly presented by the authors. Though we will outline roughly the underlying argument here.

First define a sufficient statistic  $f$  to be  $k$ -homogeneous if  $\exists k \in \mathbb{R}_+$  such that,

$$f(\eta x) = \eta^k f(x), \forall x \in \mathbb{R}^N, \forall \eta > 0. \quad (26)$$

All norms, composite norms and composition of norms with linear operators are 1-homogeneous – and so our  $\ell_1$ -norm has  $k$  of 1. If a sufficient statistic  $f$  is  $k$ -homogeneous, then the normalization factor  $C(\mu)$  of  $p(\kappa|\mu)$  is given by (Pereyra et al. 2015),

$$C(\mu) = A\mu^{-N/k}, \quad (27)$$

where  $A$  is a constant independent from  $\mu$ . The proposed Bayesian inference model then implements a gamma-type hyper-prior –

which is a typical hyper-prior for scale-parameters,

$$p(\mu) = \frac{\beta^\alpha}{\Gamma(\alpha)} \mu^{\alpha-1} e^{-\beta\mu} \mathbb{I}_{\mathbb{R}_+}(\mu), \quad (28)$$

where without loss of generality  $\alpha = \beta = 1$ . The result is effectively insensitive to their value (in numerical experiments values of  $\alpha, \beta \in [10^{-2}, 10^5]$  produced essentially no difference in  $\mu$ ).

Now, let us extend the inference problem of the log-posterior to the case where  $\mu$  is an additionally unknown parameter. In this context we compute the joint MAP estimator  $(\kappa^{\text{map}}, \mu^{\text{map}}) \in \mathbb{C}^N \times \mathbb{R}_+$  which maximizes  $p(\kappa, \mu|\gamma)$  such that,

$$\mathbf{0}_{N+1} \in \partial_{\kappa, \mu} \log p(\kappa^{\text{map}}, \mu^{\text{map}}|\gamma), \quad (29)$$

where  $\mathbf{0}_i$  is the  $i$ -dimensional null vector and  $\partial_s h(s')$  is the set of sub-gradients of function  $h(s)$  at  $s'$ . This in turn implies both that,

$$\mathbf{0}_N \in \partial_\kappa \log p(\kappa^{\text{map}}, \mu^{\text{map}}|\gamma), \quad (30)$$

and

$$\mathbf{0} \in \partial_\mu \log p(\kappa^{\text{map}}, \mu^{\text{map}}|\gamma). \quad (31)$$

From equation (30) we recover the optimization problem with known regularization parameter  $\mu$  given in equation (20). However, from equations (27, 28, 31) it follows that the MAP regularization parameter  $\mu$  is given by (Pereyra et al. 2015),

$$\mu^{\text{map}} = \frac{\frac{N}{k} + \alpha - 1}{f(\kappa^{\text{map}}) + \beta}, \quad (32)$$

where we recall that  $N$  is the total dimension of our convergence space.

It is precisely this optimal  $\mu$  value which we wish to use in our hierarchical Bayesian model. Hereafter we drop the map superscript from  $\mu$  for clarity. To calculate  $\mu$  we perform preliminary iterations defined by:

$$\kappa^{(t)} = \operatorname{argmin}_\kappa \left\{ f(\kappa; \mu^{(t)}) + g(\kappa) \right\}, \quad (33)$$

where  $g(\kappa)$  is our likelihood term and,

$$\mu^{(t+1)} = \frac{\frac{N}{k} + \alpha - 1}{f(\kappa^{(t)}) + \beta}. \quad (34)$$

Typically we find that these preliminary iterations take  $\sim 5\text{-}10$  iterations to converge, and recover close to optimal parameter selection for a range of test cases – note that here the optimal selection of  $\mu$  is that which maximizes the SNR of a recovered image.

Another factor which can influence the quality of reconstructions is the selection of wavelet dictionary. In this paper we consider Daubechies (8 levels) and SARA dictionaries (Carrillo et al. 2012, 2013), though a wide variety of wavelet dictionaries exist, see e.g. starlets (Starck et al. 2015). The 8-level SARA dictionary is a combination of the Dirac and Daubechies 1 to 8 wavelet dictionaries. It is important to note that we use the SARA dictionary, not the complete SARA scheme (Carrillo et al. 2012, 2013), which involves an iterative re-weighting scheme that is not considered here.

### 3.5 Super-Resolution Image Recovery

Gridding of weak lensing data is advantageous in that it can provide a good understanding of the noise properties – a necessary feature for principled uncertainty quantification. However, an inherent drawback of projecting data into a grid is the possibility of creating an incomplete space due to low sampling density – often

referred to as masking. Decomposition of spin signals on bounded manifolds is inherently degenerate (Bunn et al. 2003b); specifically the orthogonality of eigenfunctions is locally lost at the manifold boundaries, leading to signal leakage between Fourier (or on the sphere, harmonic) modes.

One approach to mitigate this problem is to avoid the necessity of gridding by substituting a *non-uniform discrete Fourier transform* (NFFT) into the RHS of equation (16) as presented by Lanusse et al. (2016). A downside of this NFFT approach is that the noise is more difficult to handle, leading to complications when considering uncertainty quantification. Another approach is to perform super-resolution image recovery, which we present in the context of our algorithm.

Suppose the dimension of our gridded measurement space is  $M$ , as before, and the desired dimension of our solution space is  $N'$ , where  $N' \geq N$ . In this setting we have shear measurements  $\gamma \in \mathbb{C}^M$  and recovered convergence  $\kappa \in \mathbb{C}^{N'}$ . Let us now define a *super-resolution* (subscript SR) measurement operator to be,

$$\Phi_{\text{SR}} = \mathbf{M} \mathbf{F}_{\text{lr}}^{-1} \mathbf{D} \mathbf{Z} \mathbf{F}_{\text{hr}} \quad (35)$$

where  $\mathbf{F}_{\text{hr}}$  is a high resolution (dimension  $N'$ ) fast Fourier transform,  $\mathbf{Z} \in \mathbb{C}^{N \times N'}$  is a Fourier space down-sampling which maps  $\tilde{\kappa}' \in \mathbb{C}^{N'}$  on to  $\tilde{\kappa} \in \mathbb{C}^N$ , where tilde represents Fourier coefficients,  $\mathbf{D}$  is the planar forward model given by equation (11), and  $\mathbf{M}$  is a standard masking operator. Finally,  $\mathbf{F}_{\text{lr}}^{-1}$  is a low resolution (dimension  $M$ ) inverse fast Fourier transform. For completeness the super-resolution adjoint measurement operator is given by,

$$\Phi_{\text{SR}}^\dagger = \mathbf{F}_{\text{hr}}^{-1} \mathbf{Z}^\dagger \mathbf{D}^\dagger \mathbf{F}_{\text{lr}} \mathbf{M}^\dagger, \quad (36)$$

where  $\mathbf{M}^\dagger$  is adjoint masking (gridding),  $\mathbf{D}^\dagger$  is the adjoint of  $\mathbf{D}$  (which is self-adjoint hence  $\mathbf{D}^\dagger = \mathbf{D}$ ), and  $\mathbf{Z}^\dagger \in \mathbb{C}^{M' \times M}$  is zero padding in Fourier space which acts by mapping  $\tilde{\gamma} \in \mathbb{C}^M$  to  $\tilde{\gamma}' \in \mathbb{C}^{M'}$ . Note that when considering the KS estimate in the super-resolution setting a rescaling function to account for the different Fourier normalization factors must be introduced (which we absorb into the Fourier operators). As before, this super-resolution measurement operator is concatenated with the inverse covariance weighting to form an analogous composite operator  $\bar{\Phi}_{\text{SR}}$  which is used throughout the following analysis.

Conceptually super-resolution allows partial inpainting of higher resolution Fourier modes. In this way one is able to recover high resolution structure for images from comparatively low resolution datasets. Such high resolution structure is of course dependent on the prior information injected when solving the inverse problem. Interestingly this raises another consideration: in scenarios where the pixel-level observation count is very low the noise level dilutes high frequency components and can limit the efficacy of reconstruction algorithms. In such a setting gridding observational data onto a lower resolution map, with inherently lower pixel-level noise, and performing a super-resolution reconstruction can recover far better estimates of the high frequency modes, and thus often recovers greater reconstruction fidelity.

#### 4 BAYESIAN UNCERTAINTY QUANTIFICATION

Estimators recovered from algorithms of the form presented in the previous section are MAP solutions to, in general, ill-conditioned inverse problems, and as such have significant intrinsic uncertainty. Theoretically, MCMC techniques could be applied to recover the complete posterior in the context of Gaussian (Alsing et al. 2016; Schneider et al. 2015) and sparsity-promoting (Cai et al. 2017a;

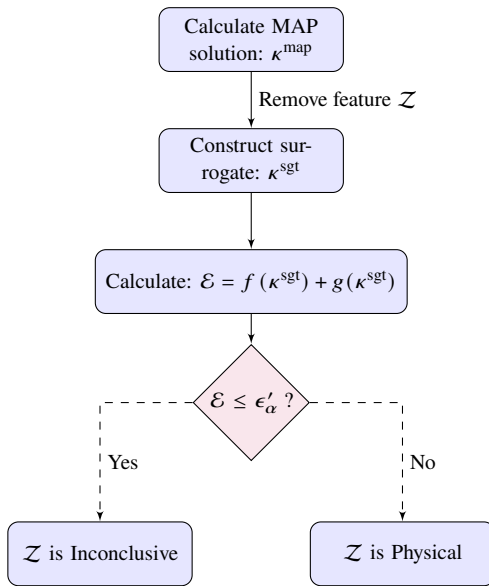


**Figure 2.** Schematic of hypothesis testing. The feature  $Z$  is entirely general and can be constructed by any well defined operator on the MAP solution  $\kappa^{\text{map}}$ .

Pereyra 2013) priors but these approaches are computationally demanding for high dimensional problems where  $N$  is large. As  $N$  can easily be larger than  $10^6$  (e.g. when considering  $1024 \times 1024$  resolution images), MCMC approaches are often not feasible.

In Pereyra (2017) a methodology based on probability concentration is presented, which uses MAP estimators to estimate theoretically conservative approximate Bayesian credible regions (specifically highest posterior density credible regions) of the posterior,  $p(\kappa|\gamma)$ . As this approach requires only knowledge of the MAP solution and the objective function, the Bayesian credible regions can be approximated efficiently in high dimensional settings.

#### 4.1 Highest Posterior Density Regions

A posterior credible region at confidence level  $100(1 - \alpha)\%$  is a sub-set  $C_\alpha \in \mathbb{C}^N$  which satisfies the integral,

$$p(\kappa \in C_\alpha | \gamma) = \int_{\kappa \in \mathbb{C}^N} p(\kappa | \gamma) \mathbb{I}_{C_\alpha} d\kappa = 1 - \alpha, \quad (37)$$

where  $\mathbb{I}_{C_\alpha}$  is the set indicator function for  $C_\alpha$  defined by  $\mathbb{I}_{C_\alpha}(\kappa) = 1 \forall \kappa \in C_\alpha$  and 0 elsewhere. One possible region which satisfies this property is the *Highest Posterior Density* (HPD) region defined by,

$$C_\alpha := \{\kappa : f(\kappa) + g(\kappa) \leq \epsilon_\alpha\}, \quad (38)$$

where  $\epsilon_\alpha$  defines an iso-contour (*i.e.* level-set) of the log-posterior set such that the integral in (37) is satisfied. This region can be shown (Robert 2001) to have minimum volume and is thus decision-theoretically optimal. However, due to the dimensionality of the integral in (37) calculation of the HPD credible region is difficult. A conservative approximation of  $C_\alpha$  was recently proposed (Pereyra 2017) and shown to be effective in the inverse imaging setting of radio interferometric imaging (Cai et al. 2017b). This approximate HPD is defined by

$$C'_\alpha := \{\kappa : f(\kappa) + g(\kappa) \leq \epsilon'_\alpha\}, \quad (39)$$

where the approximate threshold  $\epsilon'_\alpha$  is given by

$$\epsilon'_\alpha = f(\kappa^{\text{map}}) + g(\kappa^{\text{map}}) + \tau_\alpha \sqrt{N} + N, \quad (40)$$

with constant  $\tau_\alpha = \sqrt{16 \log(3/\alpha)}$ . For a detailed derivation of this approximation see Pereyra (2017). Provided  $\alpha \in (4 \exp(-N/3), 1)$  the deviation of this adapted threshold is bounded and grows at most linearly with respect to  $N$ . The error of this approximate threshold is bounded by

$$0 \leq \epsilon'_\alpha - \epsilon_\alpha \leq \eta_\alpha \sqrt{N} + N, \quad (41)$$

where  $\eta_\alpha = \sqrt{16 \log(3/\alpha)} + \sqrt{1/\alpha}$ . In high dimensional settings ( $N$  large) this error may naively appear large, however in practice the error is relatively small.

## 4.2 Hypothesis Testing

Extending the concept of HPD credible regions, one can perform *knock-out* hypothesis testing of the posterior to determine the physicality of recovered structure (Cai et al. 2017b).

To perform such tests one first creates a surrogate image  $\kappa^{\text{sgt}}$  by masking a feature of interest  $\Omega_D \subset \Omega$  in the MAP estimator  $\kappa^{\text{map}}$ . It is then sufficient to check if,

$$f(\kappa^{\text{sgt}}) + g(\kappa^{\text{sgt}}) \leq \epsilon'_\alpha. \quad (42)$$

If this inequality holds, we interpret that the physicality of  $\Omega_D$  is undetermined and so no strong statistical statement can be made. Should the objective function evaluated at  $\kappa^{\text{sgt}}$  be larger than  $\epsilon'_\alpha$  then it no longer belongs to the approximate credible set  $C'_\alpha$  and therefore (as  $\epsilon'_\alpha$  is conservative) it **cannot** belong to the HPD credible set  $C_\alpha$ . Therefore, for  $\kappa^{\text{sgt}}$  which do not satisfy the above inequality we determine the structure  $\Omega_D$  to be strictly physical at  $100(1 - \alpha)\%$  confidence level. A schematic of hypothesis testing is provided in Figure 2.

In pixel-space we begin by masking out a feature of interest, creating a rough surrogate image – setting the pixels associated with a selected structure to 0 – this rough surrogate is then passed through an appropriate wavelet filter  $\Lambda$  as part of *segmentation-inpainting* to replace generic background structure into the masked region. Mathematically, this amounts to the iterations,

$$\kappa^{(i+1),\text{sgt}} = \kappa^{\text{map}} \mathbb{I}_{\Omega - \Omega_D} + \Lambda^\dagger \text{soft}_{\lambda_t}(\Lambda \kappa^{(i),\text{sgt}}) \mathbb{I}_{\Omega_D}, \quad (43)$$

where  $\Omega_D \subset \Omega$  is the sub-set of masked pixels,  $\mathbb{I}_{\Omega - \Omega_D}$  is the set indicator function and  $\lambda_t$  is a thresholding parameter which should be chosen appropriately for the image.

A second straightforward method for generating surrogate images is to blur local pixel substructure into one collective structure – in a process called *segmentation-smoothing*. This approach provides a simple way to determine if the substructure in a given region is physical or likely to be an artifact of the reconstruction process.

For example, if several massive peaks are located near one another, one can blur these structures into a single cohesive peak. This would be useful when considering peak statistics on convergence maps – which is often used to constrain the cosmological parameters associated with dark matter.

One can conduct such blurring of structure by: specifying a subset of the reconstructed pixels  $\Omega_D \subset \Omega$ ; convolving  $\kappa^{\text{map}}$  with a Gaussian smoothing kernel; and replacing pixels that belong to  $\Omega_D$  with their smoothed counterparts. This can be displayed algorithmically as,

$$\kappa^{\text{sgt}} = \kappa^{\text{map}} \mathbb{I}_{\Omega - \Omega_D} + (\kappa^{\text{map}} * \mathcal{G}(0, \chi)) \mathbb{I}_{\Omega_D}, \quad (44)$$

where  $\mathcal{G}(0, \chi)$  is a chosen Gaussian smoothing kernel and  $*$  is a trivially extended 2D version of the the usual 1D Fourier convolution operator,

In the scope of this paper we focus primarily on pixel-space features, but it is important to stress that *knock-out* approach is entirely general and can be applied to any well defined feature of a MAP estimator – *i.e.* masking certain Fourier space features, removal of global small scale structure *etc.*

## 5 ILLUSTRATION ON SIMULATIONS

We now consider a selection of realistic simulations to illustrate our sparse reconstruction method on cluster scales which are particularly challenging for myriad factors. Further to this, we showcase the aforementioned uncertainty quantification methods in a variety of idealized cluster scale MAP reconstructions. We place emphasis on uncertainty quantification rather than the reconstruction fidelity.

### 5.1 Datasets

In this paper we focus primarily on 4 large clusters (those with significant friends-of-friends, *i.e.* significant substructure) extracted from the Bolshoi N-body simulation (Klypin et al. 2011). On the cluster scale we showcase our formalism on a variety of Bolshoi N-body simulation data sets. The Bolshoi N-body cluster simulation catalogs we work with in this paper are those used in Lanusse et al. (2016), which were extracted using the CosmoSim web-tool<sup>1</sup>. Construction of these weak lensing realisations assumed a redshift of 0.3, with a  $10 \times 10$  arcmin<sup>2</sup> field of view, and have convergence normalized with respect to lensing sources at infinity. Explicitly this results in pixel-dimensions of  $\sim 2.5$  arcseconds. Due to the relatively low particle density, these images were subsequently denoised by a multi-scale Poisson denoising algorithm.

### 5.2 Methodology

Typically, we begin by creating an artificial shear field  $\hat{\gamma} \in \mathbb{C}^M$  from a known *ground-truth* convergence field  $\kappa$ , that is extracted from a given dataset. This is a common approach in the imaging community and presents a closed scenario in which the true input is known. These  $\hat{\gamma}$  fields are created by,

$$\hat{\gamma} = \Phi \kappa + \mathcal{N}(0, \sigma_i^2), \quad (45)$$

where  $\sigma_i$  (*i.e.* the noise covariance) is determined entirely from a pre-defined number density of observations  $n_{\text{gal}}$  per arcminute<sup>2</sup>, an assumed intrinsic ellipticity dispersion of 0.37, and the resolution of the images (in this case  $10 \times 10$  arcminutes). In this way the noise can be tuned to directly mimic that present in practical settings. Using the simulated noise covariance (which in practice would be provided by the observation team) we then utilize the SOPT<sup>2</sup> framework to perform our reconstruction algorithm on  $\hat{\gamma}$  such that we recover a MAP estimator of the convergence  $\kappa^{\text{map}}$ . From this reconstructed convergence field a recovered SNR is computed and a selection of hypothesis tests are conducted to showcase the power of this formalism.

In the case where the underlying clean  $\gamma$  are unavailable (*i.e.*

<sup>1</sup> <https://www.cosmosim.org>

<sup>2</sup> A highly optimized sparse optimization solver, <https://github.com/astro-informatics/SOPT>

**Table 1.** Contains both reconstruction SNR and Pearson correlation coefficient (topological correlation) metrics for the raw KS (no smoothing), an optimally smoothed KS (grid search for smoothing kernel which maximizes the recovered SNR), and our sparse reconstructions of the Bolshoi-3 cluster simulated with realistic noise derived from the presented number density of galaxy observations  $n_{\text{gal}}$ . The difference column is calculated as the difference between the Sparse and smoothed KS recovered SNR. Note that dB is a logarithmic scale therefore increases of  $\sim 20$ dB are extreme reductions in RMS error.

Input $n_{\text{gal}}$	KS	KS Smooth	Sparse	Difference
SNR (dB)				
500	2.917	6.276	27.506	+ 21.230
100	-4.497	5.774	21.955	+ 16.181
30	-10.400	5.340	21.462	+ 16.122
10	-15.970	5.041	14.409	+ 9.368
Pearson Correlation				
500	0.166	0.902	0.977	+ 0.075
100	0.076	0.796	0.970	+ 0.174
30	0.039	0.689	0.955	+ 0.266
10	0.029	0.716	0.949	+ 0.233

application to A520 data) we conduct the same analysis as before but instead of creating artificial noisy  $\hat{\gamma}$  maps we used the real noisy observational data.

Throughout our analysis the recovered SNR (dB) is defined to be,

$$\text{SNR} = 20 \times \log_{10} \left( \frac{\|\kappa\|_2}{\|\kappa - \kappa^{\text{map}}\|_2} \right), \quad (46)$$

when the ground-truth convergence is known. Furthermore we quantify the topological similarity between the true convergence and the estimator *via* the Pearson correlation coefficient which is defined to be

$$r = \frac{\sum_{i=1}^{N_{\text{gal}}^2} \{\kappa^{\text{map}}(i) - \bar{\kappa}^{\text{map}}\} \{\kappa(i) - \bar{\kappa}\}}{\sqrt{\sum_{i=1}^{N_{\text{gal}}^2} \{\kappa^{\text{map}}(i) - \bar{\kappa}^{\text{map}}\}^2} \sqrt{\sum_{i=1}^{N_{\text{gal}}^2} \{\kappa(i) - \bar{\kappa}\}^2}}, \quad (47)$$

where  $\bar{x} = \langle x \rangle$ . The correlation coefficient  $r \in [-1, 1]$  quantifies the structural similarity between two datasets: 1 indicates maximal positive correlation, 0 indicates no correlation, and -1 indicates maximal negative correlation.

### 5.3 Bolshoi Cluster Catalogs

The Bolshoi cluster data used consists of 4 large clusters extracted from the Bolshoi N-body simulation (Klypin et al. 2011; Lanusse et al. 2016). These images were then multi-scale Poisson denoised to create suitable ground truth simulations. We choose to analyze the same clusters considered in Lanusse et al. (2016), as they showcase a wide variety of structure on all scales. Hereafter, we restrict ourselves to the SARA dictionary (Carrillo et al. 2012) truncated at the 4<sup>th</sup> Daubechies wavelet (DB4) for simplicity – *i.e.* the combination of the Dirac, and DB1 to DB4 wavelet dictionaries only.

To investigate the SNR gain of our formalism over KS in the cluster scale setting, we created realizations of noisy pseudo-shear maps for assumed number density of galaxy observations  $n_{\text{gal}} \in [500, 100, 30, 10]$  from one Bolshoi cluster map, upon which

we applied our reconstruction algorithm pipeline. The results of which are presented in Table 1. It should be noted that for comparisons sake the KS estimate without convolution with a Gaussian smoothing kernel is provided in addition to an optimally smoothed KS estimator. This has been done to highlight the difference in reconstruction fidelity between the raw KS estimator and the KS estimator after post-processing (Gaussian smoothing), a discrepancy often not addressed by the community. As this post-processing convolution is known to degrade the quality of non-Gaussian information (which cosmologists are becoming increasingly interested in) such plots demonstrate the trade-off between non-Gaussian information and reconstruction fidelity.

As can be seen in Figure 3 and Table 1, sparse approaches significantly outperform the smoothed (and non-smoothed) KS approach in all cases, over all metrics tracked. Importantly sparse approaches are able to recover reasonable results even when the noise level entirely dilutes the true signal, as in the  $n_{\text{gal}} = 10$  setting, making such approaches on (at least) cluster data very attractive for future studies.

#### 5.3.1 Hypothesis Testing: Bolshoi Clusters

Perhaps more interestingly, we now perform a series of hypothesis tests as discussed in Section 4.2. For each of the remaining 3 Bolshoi cluster we construct three possible example hypothesis tests which one may wish to perform. In this case these hypotheses were either: structure removal followed by segmentation-inpainting; or Gaussian smoothing of certain structures (*i.e.* smoothing multiple peaks into a single larger peak which may be of interest when conducting peak-count analysis). Though these are both extremely useful considerations, it is important to stress the generality of our approach such that any well defined operation on the reconstructed image, with a clear understandable hypothesis, is applicable.

To ensure the method behind hypothesis testing is clear, we will walk through a typical application. The top row of Figure 4 displays the hypothesis tests applied to the first Bolshoi cluster. Conceptually, the correct way to interpret Hypothesis 1 (H1, red) is: ‘*The central dark core is likely just an artifact of the reconstruction*’.

This structure is then removed from the image by segmentation-inpainting (lower left image), and the objective function is then recalculated. It is found that the objective function is now larger than the approximate level-set threshold  $\epsilon'_{99\%}$ , the surrogate segmentation-inpainted image falls outside of the 99% HPD credible region, and so the hypothesis is **rejected**. This implies that the structure is not simply an artifact, but is necessary to the integrity of the reconstruction, *i.e.* this structure is now determined to be physical at 99% confidence. However, had removing this region **not** raised the objective function above  $\epsilon'_{99\%}$ , then the conclusion is that their is insufficient evidence to reject the hypothesis (which is **not** equivalent to saying that the region is strictly not physical).

An identical thought process can be applied to H2 and H3 of the top row in Figure 4, H1 in the second row of Figure 4, and all three hypothesis tests presented in the final row. In each case a substructure of the  $\kappa^{\text{map}}$  is removed *via* segmentation-inpainting and it is queried whether the resulting surrogate solution  $\kappa^{\text{sgt}} \in C'_\alpha$ . Each of the large substructures on the final row, and H2 of the second row, are determined to be physical at 99% confidence. Conversely, the comparatively smaller substructures considered in H2 and H3 of the top row do not saturate the level-set threshold, and are therefore undetermined. All numerical data related to hypothesis testing of the Bolshoi cluster reconstructions can be found in Table 2.

H2 and H3 of the middle row of Figure 4 have a different

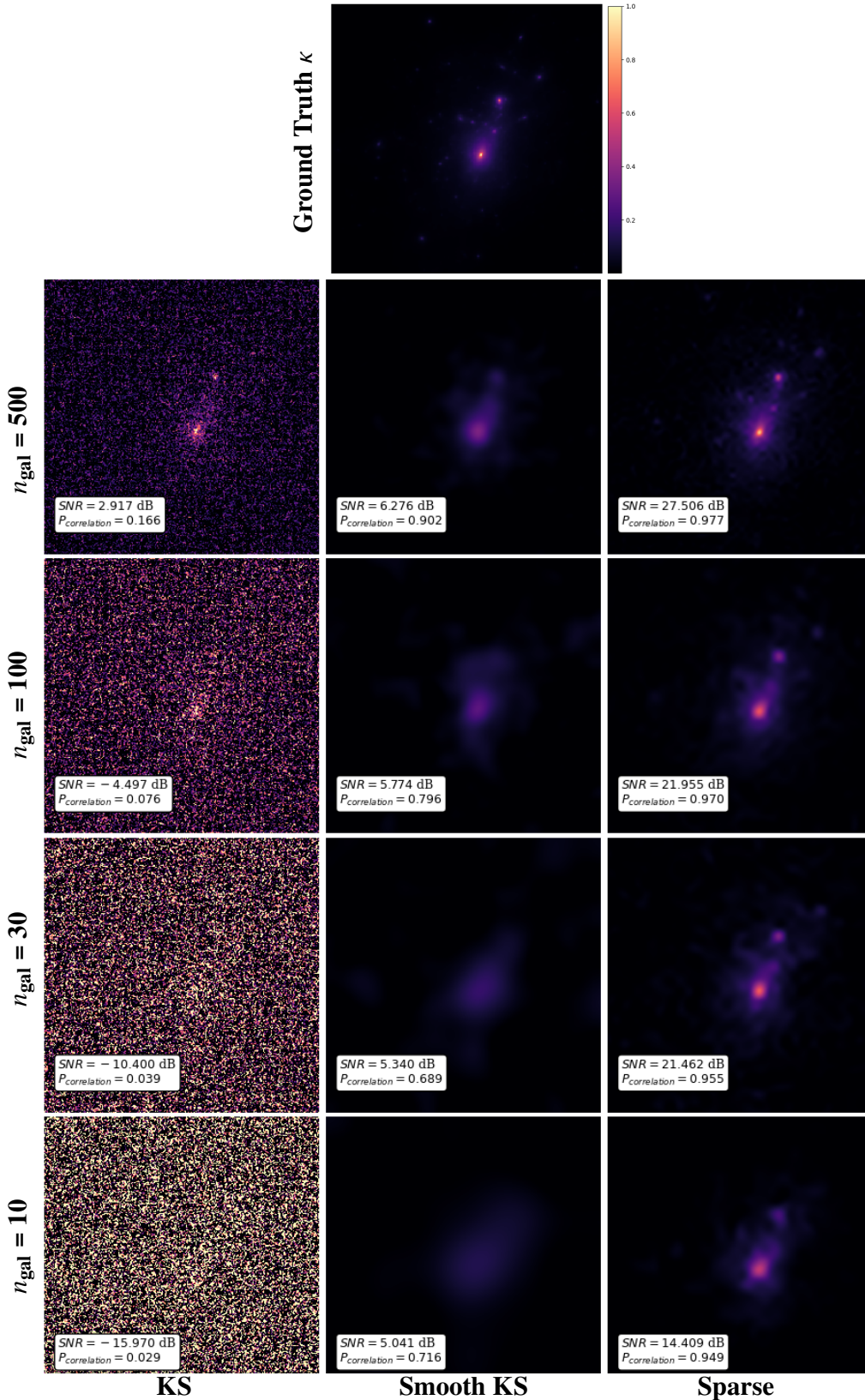


**Figure 3.** Top to bottom: Ground truth convergence map, simulations with noise levels corresponding to  $n_{\text{gal}} \in [500, 100, 30, 10]$  respectively. Notice the clear effectiveness of sparse reconstruction over the standard KS method for a range of input SNR values. The numerical details can be found in Table 1. The vertical labels indicate the input  $n_{\text{gal}}$  used to simulate realistic noise for a given row, whereas horizontal labels indicate the reconstruction type. An optimal (grid searched to maximize the recovered SNR) Gaussian smoothing kernel was applied to the KS recovery to yield the KS (smooth) recovery in an attempt to remove noise from the KS estimator (obviously this is not possible in practice, where the ground truth is unknown: results shown therefore present the best possible performance for the smoothed KS estimator). Clearly, in all cases, the super-resolution sparse approach produces convergence maps which are far more representative of the ground truth across the aforementioned metrics.

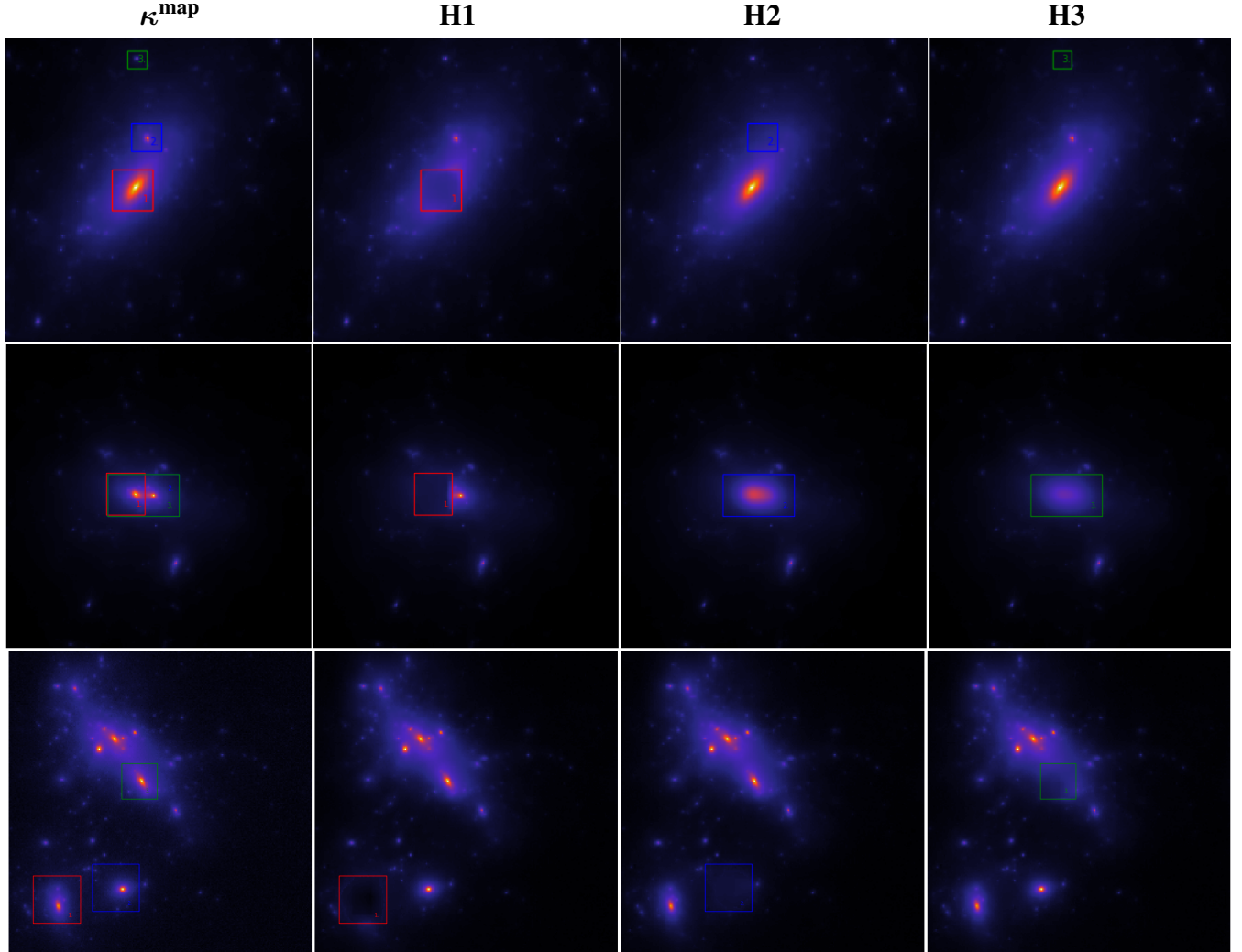


**Figure 4. General:** Hypothesis testing of three selected structures in the Bolshoi-1 cluster convergence field. The number density of galaxy observations  $n_{\text{gal}}$  was set idealistically to 500 arcminute $^{-2}$  simply for demonstration purposes. Additionally super-resolution was not active and the masking was trivially set to the identity, again to simplify the example for demonstration purposes. All numerical details can be found in Table 2. **Top row:** We correctly determine that region 1 (red) is physical with 99% confidence. Regions 2 (blue) and 3 (green) remain within the HPD region and are therefore inconclusive, given the data and noise level. **Middle row:** We correctly determine that all three null hypotheses (red, blue and green) are rejected at 99% confidence. In H1 the conclusion is that the left hand peak was statistically significant. In H2 and H3 the conclusions is that an image with the two peaks merged it unacceptable, and therefore the peaks are distinct at 99% confidence. **Bottom row:** We correctly determine that all three hypothesis regions (red, blue and green)  $\Omega_D$  are physical with 99% confidence.

interpretation. In these cases the central region has been blurred by segmentation-smoothing (convolution with a Gaussian smoothing kernel) – the difference between these two cases being simply the degree of smoothing. Here the hypothesis is: ‘The central region is likely to be just a single peak, rather than two’. As in the previous example, the objective function is recalculated and is now greater than  $\epsilon'_{99\%}$  and so the hypothesis is rejected. The natural conclusion is thus that the data is sufficient to determine that at least two peaks are physically present at 99% confidence.

## 6 APPLICATION TO ABEL-520 OBSERVATIONAL CATALOGS

We perform an application of our entire reconstruction pipeline to real observational datasets. We select two observational datasets of the A520 cluster (Jee et al. 2014; Clowe et al. 2012) – hereafter for clarity we refer to them as C12 and J14 (as in Peel et al. 2017)<sup>3</sup>. For a full description of the datasets, how they were constructed, and how they account for different systematics we recommend the reader look to the respective papers. These initial investigations claim to have detected several over dense regions within the merging A520 system, the most peculiar of which was a so called ‘dark core’ (location 2 in Figure 5) for which multi-wavelength observations

<sup>3</sup> <http://www.cosmostat.org/software/glimpse>

**Table 2.** Displays the MAP objective function, level-set threshold at 99% confidence, surrogate objective function and whether the removed region was successfully identified as being physical. This data-set corresponds to Figures 4

Test	Initial $f(\kappa) + g(\kappa)$	Threshold $\epsilon'_{99\%}$	Surrogate $f(\kappa^{sgt}) + g(\kappa^{sgt})$	Reject $H_0$ ?
<b>Bolshoi-1</b>				
H1	95426	163408	805513	✓
H2	95426	163408	134080	✗
H3	95426	163408	100582	✗
<b>Bolshoi-2</b>				
H1	97121	165103	824260	✓
H2	97121	165103	221492	✓
H3	97121	165103	366981	✓
<b>Bolshoi-3</b>				
H1	83419	151401	369939	✓
H2	83419	151401	234305	✓
H3	83419	151401	314089	✓

**Table 3.** Displays the MAP objective function, level-set threshold at 99% confidence, surrogate objective function and whether the null hypothesis  $H_0$  is rejected. As can be seen, both MAP solutions fail to reject the null hypothesis in the other's objective function. This leads us to conclude that the two datasets do not disagree at 99% confidence. Further discussion akin to the Kullback-Leibler divergence of the two posteriors is beyond the scope of this paper, but perhaps of interest in future work.

Hypothesis Test	Initial $f(\kappa) + g(\kappa)$	Threshold $\epsilon'_{99\%}$	Surrogate $f(\kappa^{sgt}) + g(\kappa^{sgt})$	Reject $H_0$ ?
$C12 \Leftrightarrow J14$	99231	168044	125601	✗
$J14 \Leftrightarrow C12$	98943	167243	134391	✗

could not determine an optical counterpart. Such a dark core would provide a contradiction to the currently understood model of collisionless dark matter – the idea being that during the collision of two massive clusters, dark matter was stripped from each cluster through self-interactions, forming an over dense residual between the two clusters, which would naturally not exhibit an optical counterpart.

The [J14](#) catalog contains approximately twice the number of galaxies than [C12](#), though both are derived from the same ACS (four pointings) and Magellan images. In addition, [J14](#) combines these images with the CFHT catalog used in the authors previous work ([Jee et al. 2012](#)). The [C12](#) observing area extends over a larger angular surface than the [J14](#) so for this analysis we limit both datasets to the region spanned by both sets. Due to the number density of measurements being very low we are forced to project the measurements into a  $32 \times 32$  grid – to ensure that the average number of galaxies in each grid pixel is at least above 1, though ideally we want many galaxies in each pixel to minimize the noise contribution from intrinsic ellipticity. In fact, even in this resolution the space is incomplete in several pixels, but we draw a compromise between the completeness of the space and the resolution of the data.

The data covariance was constructed directly from the number density of observations per pixel (directly inferred during catalogue gridding), with an assumed intrinsic ellipticity dispersion of 0.37. Combining this data covariance, the associated gridded datasets,

and the associated mask, MAP reconstructions of the [C12](#) and [J14](#) convergence maps were recovered at a super-resolution magnification of 8. Reconstructions are presented in Figure 5.

## 6.1 Hypothesis Testing of Local Structure: A520 Datasets

We conducted hypothesis tests on the three primary over dense regions, in addition to the contested dark core, in both the [C12](#) and [J14](#) datasets. In the absence of an optical counterpart, detection at high confidence of the dark core (location 2 in Figure 5) would provide a contradiction to the collisionless model of dark matter – indicating potential self-interaction of dark matter. Due to the high estimated noise-level present in the data, and the limited data resolution, only the two largest peaks in both datasets (peaks 1 and 3 of Figure 5) sufficiently raised the objective function to reject the hypothesis at any meaningful confidence. This is to say that; given the limited, noisy data and using the measurement operator and prior ( $\ell_1$ -term) presented in this paper we can say that the data is insufficient to statistically determine the physicality of local small scale substructure (such as the dark core) in both the [C12](#) and [J14](#) datasets. The initial conflict between [C12](#) and [J14](#) was over the existence and position of a dark core (location 2 in Figure 5), with a notably large mass-to-light ratio, indicated the possibility of self-interacting dark matter. A subsequent inquiry was conducted ([Peel et al. 2017](#)) using the GLIMPSE reconstruction algorithm ([Lanusse et al. 2016](#)) and concluded that this peculiar peak existed in the [J14](#) dataset but not in the [C12](#) dataset.

As such, our conclusions agree well with [Peel et al.](#) (and generally with those drawn in both [C12](#) and [J14](#)). However, within our Bayesian hierarchical formalism (which constitutes a principled statistical framework) we push this conclusion further to say that the data are insufficient to determine the physicality of these peaks.

## 6.2 Hypothesis Testing of Global Structure: A520 Datasets

Interestingly we can perform a final novel hypothesis test of global structure. This hypothesis is as follows: ‘*The two MAP estimates are consistent with both sets of data*’, i.e. the MAP convergence estimate recovered from the [J14](#) ([C12](#)) data is within the credible-set (at 99% confidence) of the [C12](#) ([J14](#)) objective function. We find that the [J14](#) ([C12](#)) MAP reconstruction is an acceptable solution to the [C12](#) ([J14](#)) inverse problem and so the MAP solutions do not disagree – numerically this is shown in Table 3.

Given the inherent limitations of the data we are forced to conclude: ‘*The data are insufficient to determine the existence of individual substructures at high confidence – though the two largest over dense regions are found to be globally physical at 99% confidence. The two MAP estimates are also found to be consistent at 99% confidence.*’

## 7 CONCLUSIONS

We have presented a sparse hierarchical Bayesian mass-mapping algorithm which provides a principled statistical framework through which, for the first time, we can conduct uncertainty quantification on recovered convergence maps without relying on any assumptions of Gaussianity. Moreover, the presented formalism draws on ideas from convex optimization (rather than MCMC techniques) which makes it notably fast and allows it to scale well to big data, i.e. high resolution and wide-field convergence reconstructions (which will be essential for future stage IV surveys, such as LSST and Euclid).

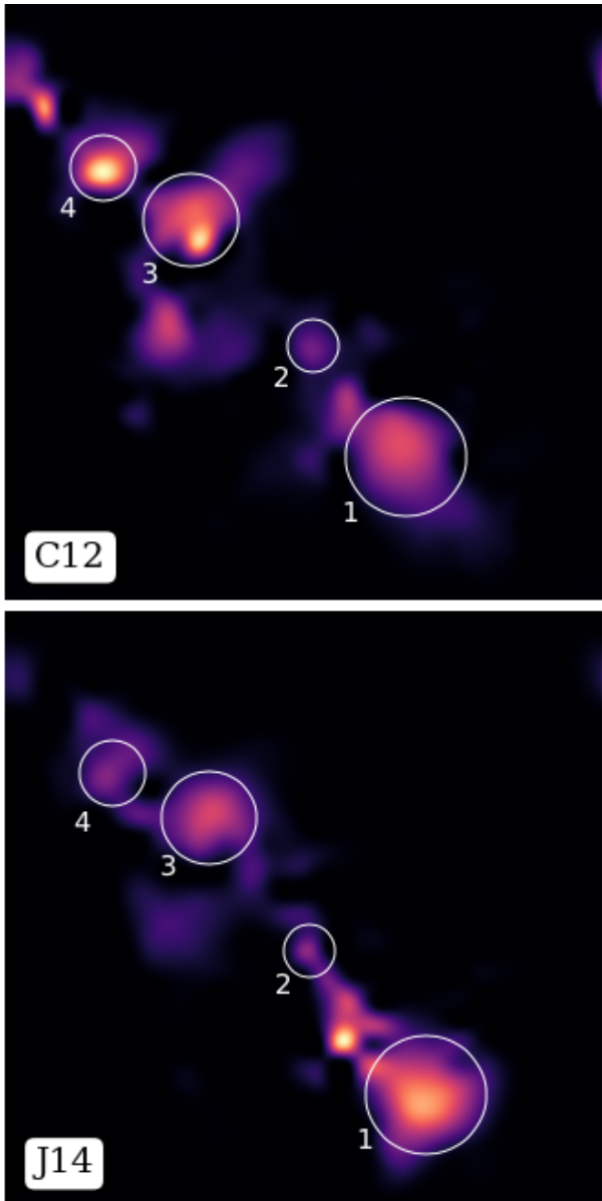


**Figure 5. Top:** Super-resolution sparse Bayesian reconstruction of J14 and C12 respectively. In a Bayesian manner it is found that the two datasets do not globally disagree at 99% confidence. However, given the data resolution and noise-levels, only peaks 1 and 3 (in both datasets) could be determined to be statistically significant. This is **not** to say they do not exist, but implies that the data quantity and quality is insufficient to make a robust, principled statistical statement which could be used as evidence of their existence. The contested peak 2 is not detected at any reasonable confidence in either dataset.

Additionally, we demonstrate a hierarchical Bayesian inference approach to automatically approximate the regularization parameter, and show that it produces near optimal results in a variety of cases. We however note that this approach does not work generally, and can be unstable in extreme settings.

We showcase our Bayesian inference approach (with emphasis on the application of the uncertainty quantification techniques) on both simulation datasets and observational data (the A520 merging cluster dataset). Our mass-mapping formalism is shown to produce significantly more accurate convergence reconstruction than

the Kaiser-Squires estimator on all simulations considered. Hypothesis tests of substructure are demonstrated.

It is found that neither of the two A520 datasets considered could provide sufficient evidence to determine the physicality of any contested substructure (*i.e.* the existence of so called ‘dark cores’) at significant confidence. It is informative to note that our methods were, in fact, sufficiently sensitive to detect the largest peaks in both datasets at 99% confidence. Nonetheless, global hypothesis tests indicate a good agreement between the two sets of data. These conclusions are roughly in agreement with those drawn previously but go further to demonstrate just how uncertain these types of cluster-scale weak lensing reconstruction inherently are (typically as a limitation of the relative information content of low-resolution, noisy datasets).

It is now natural to extend this formalism to the entire celestial sphere – a necessity of large-scale reconstruction techniques which aim to fully utilize the forthcoming Euclid and LSST<sup>4</sup> survey data.

## ACKNOWLEDGEMENTS

Author contributions are summarized as follows. MAP: methodology, data curation, investigation, software, visualization, writing - original draft; JDM: conceptualization, methodology, project administration, supervision, writing - review & editing; XC: methodology, investigation, writing - review & editing; TDK: methodology, supervision, writing - review & editing; CGRW: methodology.

This paper has undergone internal review in the LSST Dark Energy Science Collaboration. The internal reviewers were Chihway Chang, Tim Eifler, and François Lanusse. The authors would like to thank Luke Pratley for an introduction to the C++ SOPT framework and the internal reviewers for valuable discussions. MAP is supported by the Science and Technology Facilities Council (STFC). TDK is supported by a Royal Society University Research Fellowship (URF). This work was also supported by the Engineering and Physical Sciences Research Council (EPSRC) through grant EP/M0110891 and by the Leverhulme Trust. The DESC acknowledges ongoing support from the Institut National de Physique Nucléaire et de Physique des Particules in France; the Science & Technology Facilities Council in the United Kingdom; and the Department of Energy, the National Science Foundation, and the LSST Corporation in the United States. DESC uses resources of the IN2P3 Computing Center (CC-IN2P3–Lyon/Villeurbanne - France) funded by the Centre National de la Recherche Scientifique; the National Energy Research Scientific Computing Center, a DOE Office of Science User Facility supported by the Office of Science of the U.S. Department of Energy under Contract No. DE-AC02-05CH11231; STFC DiRAC HPC Facilities, funded by UK BIS National E-infrastructure capital grants; and the UK particle physics grid, supported by the GridPP Collaboration. This work was performed in part under DOE Contract DE-AC02-76SF00515.

## REFERENCES

- Alsing J., Heavens A., Jaffe A. H., Kiessling A., Wandelt B., Hoffmann T., 2016, *MNRAS*, **455**, 4452
- Bartelmann M., Schneider P., 2001, *Phys. Rep.*, **340**, 291
- Bunn E. F., Zaldarriaga M., Tegmark M., de Oliveira-Costa A., 2003a, *Phys. Rev. D*, **67**, 023501

<sup>4</sup> <https://www.lsst.org>

- Bunn E. F., Zaldarriaga M., Tegmark M., de Oliveira-Costa A., 2003b, *Phys. Rev. D*, **67**, 023501
- Cai X., Pereyra M., McEwen J. D., 2017a, preprint, ([arXiv:1711.04818](#))
- Cai X., Pereyra M., McEwen J. D., 2017b, preprint, ([arXiv:1711.04819](#))
- Carrillo R. E., McEwen J. D., Wiaux Y., 2012, *MNRAS*, **426**, 1223
- Carrillo R. E., McEwen J. D., Van De Ville D., Thiran J.-P., Wiaux Y., 2013, *IEEE Signal Processing Letters*, **20**, 591
- Chang C., et al., 2018, *MNRAS*, **475**, 3165
- Clowe D., Bradač M., Gonzalez A. H., Markevitch M., Randall S. W., Jones C., Zaritsky D., 2006, *ApJ*, **648**, L109
- Clowe D., Markevitch M., Bradač M., Gonzalez A. H., Chung S. M., Massey R., Zaritsky D., 2012, *The Astrophysical Journal*, **758**, 128
- Coles P., Chiang L.-Y., 2000, *Nature*, **406**, 376
- Combettes P. L., Pesquet J.-C., 2009, preprint, ([arXiv:0912.3522](#))
- Corless V. L., King L. J., Clowe D., 2009, *MNRAS*, **393**, 1235
- Heavens A., 2009, *Nuclear Physics B Proceedings Supplements*, **194**, 76
- Horowitz B., Seljak U., Aslanyan G., 2018, arXiv preprint arXiv:1810.00503
- Jee M. J., Mahdavi A., Hoekstra H., Babul A., Dalcanton J. J., Carroll P., Capak P., 2012, *ApJ*, **747**, 96
- Jee M. J., Hoekstra H., Mahdavi A., Babul A., 2014, *ApJ*, **783**, 78
- Jeffrey N., et al., 2018, preprint, ([arXiv:1801.08945](#))
- Jullo E., Pires S., Jauzac M., Kneib J.-P., 2014, *Monthly Notices of the Royal Astronomical Society*, **437**, 3969
- Kaiser N., Squires G., 1993, *ApJ*, **404**, 441
- Kilbinger M., 2015, *Reports on Progress in Physics*, **78**, 086901
- Klypin A. A., Trujillo-Gomez S., Primack J., 2011, *ApJ*, **740**, 102
- Lanusse F., Starck J.-L., Leonard A., Pires S., 2016, *A&A*, **591**, A2
- Leonard A., Lanusse F., Starck J.-L., 2014, *MNRAS*, **440**, 1281
- Mediavilla E., Muñoz J. A., Garzón F., Mahoney T. J., 2016, *Astrophysical Applications of Gravitational Lensing*
- Munshi D., Coles P., 2017, *J. Cosmology Astropart. Phys.*, **2**, 010
- Munshi D., Valageas P., van Waerbeke L., Heavens A., 2008, *Phys. Rep.*, **462**, 67
- Padmanabhan N., Seljak U., Pen U. L., 2003, *New Astron.*, **8**, 581
- Paykari P., Lanusse F., Starck J.-L., Sureau F., Bobin J., 2014, *Astronomy and Astrophysics*, **566**
- Peel A., Lanusse F., Starck J.-L., 2017, *ApJ*, **847**, 23
- Pereyra M., 2013, preprint, ([arXiv:1306.0187](#))
- Pereyra M., 2017, *SIAM Journal on Imaging Sciences*, **10**, 285
- Pereyra M., Bioucas-Dias J., Figueiredo M., 2015, Maximum-a-posteriori estimation with unknown regularisation parameters. pp 230–234, doi:10.1109/EUSIPCO.2015.7362379
- Piras D., Joachimi B., Schäfer B. M., Bonamigo M., Hilbert S., van Uitert E., 2018, *MNRAS*, **474**, 1165
- Pires S., Starck J.-L., Amara A., 2009, *Monthly Notices of the Royal Astronomical Society*, **395**, 1265
- Robert C.-P., 2001, The Bayesian Choice, doi:<https://doi.org/10.1007/bf03877159>-1
- Schneider P., 2005, ArXiv Astrophysics e-prints,
- Schneider M. D., Hogg D. W., Marshall P. J., Dawson W. A., Meyers J., Bard D. J., Lang D., 2015, *ApJ*, **807**, 87
- Starck J.-L., Murtagh F., Fadili J., 2015, *Sparse Image and Signal Processing: Wavelets and Related Geometric Multiscale Analysis*
- Taylor P. L., Kitching T. D., McEwen J. D., Tram T., 2018, preprint, ([arXiv:1804.03668](#))
- Troxel M. A., Ishak M., 2015, *Phys. Rep.*, **558**, 1
- VanderPlas J. T., Connolly A. J., Jain B., Jarvis M., 2011, *ApJ*, **727**, 118
- Wallis C. G. R., McEwen J. D., Kitching T. D., Leistedt B., Plouviez A., 2017, preprint, ([arXiv:1703.09233](#))

This paper has been typeset from a Te<sub>X</sub>/La<sub>T</sub>E<sub>X</sub> file prepared by the author.